LUND UNIVERSITY

Atomistic assessment of interfacial interaction potential in tungsten twist grain boundaries

Hiremath, Praveenkumar; Melin, Solveig; Olsson, Pär

Full length article

Atomistic assessment of interfacial interaction potential in tungsten twist grain boundaries

Praveenkumar Hiremath [a] [ID],*, Solveig Melin [a], Pär A.T. Olsson [a,b] [ID]

[a] *Division of Mechanics, Materials & Component Design, Lund University, Box 118, Lund, SE-221 00, Sweden*
[b] *Materials Science and Applied Mathematics, Malmö University, SE-205 06 Malmö, Sweden*

A B S T R A C T

The present study focuses on the computation of interfacial excess potential for the cohesive zones through which a brittle crack propagates in tungsten (W) twist grain boundaries (TGBs). Additionally, the influence of phosphorus (P) impurities is investigated. To this end, we have performed classical atomistic modeling of several $\langle 110 \rangle$ TGBs in their pristine and P-impurity segregated states. The modeling entails a mode-I stress intensity factor (K_I) controlled quasi-static loading setup, in which the cohesive zone is divided into small cohesive zone volume elements (CZVEs) that enable the measurement of the scale-independent interfacial excess energy potential associated with cleavage surfaces. The study shows that the cracks in all pristine TGBs exhibit brittle failure by advancing along the GB interface. The same fracture mechanism is also observed upon the introduction of P impurities. However, debris in the form of clustered W-P agglomerates is occasionally observed on the cleavage surfaces. As for the measured excess interface energy potential, it is independent of the height chosen for the CZVEs and their position relative to the initial crack tip. This makes it useful to quantify the P induced embrittlement of TGBs and for up-scaling the results for e.g. meso-scale continuum modeling. The presence of P impurities reduces the interfacial binding energy and the associated peak stress, which is an indication of GB embrittlement. These results are in line with the experimentally observed P induced GB embrittlement in W, previously reported in the literature.

1. Introduction

The deformation behavior of polycrystalline materials is greatly influenced by the underlying microstructure, where aspects such as inclusions, voids, variation of grain size and shape, grain boundary (GB) type, texture, dislocation density, etc. play central roles for the response [1–3]. Of these microstructural features, GBs are particularly interesting because they behave as strong sinks for defects like dislocations and impurities. For brittle materials, GBs tend to be the preferred regions for cracks to propagate along, which makes their cohesive properties important for the macroscopic integrity of components [4]. Moreover, the segregation of impurities may influence the macroscopic load response of polycrystalline materials. They induce local variations in the cohesive properties, thereby either strengthening or weakening the GBs. Thus, the cohesive strength of GBs impacts the ductility of materials [5–7] and consequently the brittle to ductile transition temperature (BDTT) [8]. Therefore, understanding the GB decohesion energetics associated with the segregated impurities is paramount.

Experimental characterization of the mechanical response of individual GBs is difficult to achieve. Therefore, different computational techniques have been adopted over the years to gain insight into the phenomenon. Electronic methods like density functional theory (DFT) are typically used to probe the GB decohesion energetics associated with brittle fracture. They are used to compute the ideal work of separation (W_{sep}^{GB}) through either relaxed or unrelaxed (rigid) separation modeling of the two neighboring grains forming a GB. The correlation between the W_{sep}^{GB} and the GB segregated impurity concentration reveals the latter's influence on the GB cohesion. But, allowing atomic relaxation during these simulations results in a simulation cell size effect on the traction–separation (TS) law [9–11]. This size-dependent behavior is attributed to the uniform separation of all the atomic layers in the tensile direction and bulk elastic strain energy release during the simulation [9].

To overcome this issue, Van der Ven and Ceder [12] introduced the concept of excess properties to describe the thermodynamics of interfacial decohesion. This enabled them to separate the strain energy associated with the gradual breaking of atomic bonds at the interface from the bulk strain energy, which allowed for the parameterization of a size-independent interfacial TS excess potential. This was achieved

---

* Corresponding author.

E-mail address: praveenkumar.hiremath@lth.lu.se (P. Hiremath).

by isolating the elastic energy of $(n-1)$ homogeneously strained planes from the energy of the supercell with n homogeneously strained planes. They applied the approach to study the decohesion along a {111} plane that contained varying amounts of segregated hydrogen and oxygen, using fully relaxed DFT uniaxial tensile simulations. The procedure was found to capture the influence of impurities on the cohesive zone and recovered the universal binding energy relation (UBER) proposed by Rose et al. [13]. The same approach was adopted by Olsson and Blomqvist [14], Guzman et al. [15] and Toijer et al. [16] to investigate the impact of different types of impurities on the brittle failure of tungsten (W), iron and nickel GBs, respectively. However, an aspect that is not accounted for in such models, is that when impurities segregate at a crack tip, they complicate the crack tip behavior by influencing the local cohesive properties [17,18]. Therefore the prescribed crack plane generally does not correspond to the preferred path of propagation for cracks in GBs, because of the emergence of alternative preferential crack paths that may occur due to the interplay of impurities. Thus, an approach that does not necessitate the crack to be constrained onto a predefined crystallographic plane is desirable.

Classical atomistic methods like displacement controlled tensile molecular dynamics simulations do not require prescribing a crack plane and can shed light on impurity-driven GB fracture behavior. In these simulations, finite cracks, such as center-crack tension specimens, are subjected to tensile loading. Using this approach, McDowell et al. [19] and Yamakov et al. [20] investigated the GB cohesion in terms of stress versus separation profiles of GB interfaces (also identified as cohesive zones) in copper and aluminum GBs, respectively. In particular, Yamakov et al. [20] divided the cohesive zone of a GB into cohesive zone volume elements (CZVEs) and extracted the stress-separation relationship for the GB cohesive zone constitutive law. Analogously, based on the local stress-separation relation from CZVEs, Barrows et al. [21] investigated the change in cohesive strength of nickel GBs on account of segregated hydrogen impurities.

Over the years, many atomistic works involving quasi-static mode-I stress intensity (K_I)-controlled displacement loading of semi-infinite crack setups have been published in the literature, see e.g. [22–28] and the references therein. They satisfy the necessary conditions for linear elastic fracture mechanics (LEFM) applicability and the associated K_I-controlled displacement fields can be employed in GB setups where the reflection symmetry across the GB interface is preserved, e.g. in symmetric-tilt GBs or twist GBs (TGBs). Furthermore, a crack subjected to mode-I displacement controlled loading experiences stable growth [17,29,30]. However, a limitation is that the fracture toughness (critical stress intensity factor, K_{IC}^R) obtained from such quasi-static simulations as the K_I at which crack starts to grow is not unique [31], due to the varying atomic bond strength along a GB structural unit. Thus, for a representative estimation of the fracture toughness for post-initial crack propagation, it is required to re-compute the fields using an updated crack tip position. This is usually avoided, especially in the presence of segregated impurities, as they may produce curved crack fronts, which make the determination of the crack-tip location non-unique. Even if this were to be done, the presence of impurities alters the strength and length of the atomic bonds across the GB interface, which does not translate to the boundary displacements. As a result, the measured K_{IC}^R may not capture the actual impact of impurities.

A promising approach to probe the mode-I fracture behavior of GBs containing heterogeneities (impurities, cavities or other defects) was proposed by Tanguy [32]. They assessed the fracture toughness by fitting the shear stress field ahead of the crack-tip to an analytical solution [32,33], which yielded a good agreement between the computed fracture toughness and the theoretical Griffith prediction. As another workaround to these issues, by adopting the concept of CZVEs from [19,20], the average energy release rate, G_I, was measured instead of K_{IC}^R to understand the average fracture toughness of the pristine and impurity inhabited GBs in [31]. Here, G_I was taken as the average of all the energy release rate values, G_I^{CZ} of individual

CZVEs. However, the measured G_I^{CZ} depends on the CZVE height, thanks to the increasing contribution from the bulk to the strain energy with increasing CZVE volume [9,10]. Because the decohesion involves breaking of bonds between the two adjacent planes, bulk contributions to G_I^{CZ} should be omitted to achieve a CZVE height independent behavior for G_I^{CZ}. This was achieved by unloading the crack specimen until the initial crack tip configuration, before loading, was regained. As a result, the G_I and K_{IC} evaluations in [31] were independent of the CZVE height.

Despite the usefulness of this approach in finding the average fracture toughness of pristine and impurity segregated GBs, the extraction of decohesion laws like UBER and derivation of TS laws from it, were infeasible. Such relations are necessary to upscale the nano-scale behavior for e.g. meso-scale modeling. Möller et al. [24] presented a semi-analytical scheme to extract TS laws for the region ahead of a single crystal crack tip, based on the atomic forces in the region computed using molecular statics (MS). They even proposed a strategy for the usage of these atomistic TS laws in continuum fracture modeling [24]. However, as they stated, the scheme may not work directly for GBs, as the strength of the atomic bonds varies depending on the considered location in the GB structural unit. Such variations are expected to be further enhanced whenever the GB contains randomly dispersed impurities, which highlights the need for alternative strategies.

Considering the challenges associated with the prediction of fracture toughness for GB cracks and based on the works [20,21,24,32], it would be more meaningful to compute how properties such as stresses, forces, energy release rate, etc. that relate to the cohesion of the interface change upon introduction of impurities. Therefore, the current work presents a scheme to extract interfacial excess potentials (linked to the interface cohesion) associated with brittle failure of impurity segregated GB cracks under quasi-static K_I-loading. It is based on the approach involving CZVEs described in [31] coupled with measurement of excess (herein interface) potential as proposed by Van der Ven and Ceder [12]. Such strategies to estimate the interfacial interaction potential has – to the best of the authors' knowledge – not been adopted in the atomistic modeling of brittle GB cracks with impurities. The method is tested for the W TGBs with and without segregated phosphorus (P) impurities and gives an upper bound approximation of the energy release rate. But through a corrective scaling, based on unloading of the cracked geometry, the interfacial potential can be adjusted to predict accurate energy release rate levels. Specifically, we have chosen ⟨110⟩ TGBs for two reasons: (i) they all have the same GB interface plane, i.e. {110}, with the lowest surface energy, and (ii) their fracture studies are scarce.

The paper is structured as follows: Firstly, we provide the procedure for generating atomistic ground state geometries for pristine and P inhabited TGBs. This is succeeded by the description of the fitting procedure of an UBER for the interfacial interaction potential to describe excess interfacial energy. The utility of the outlined procedure to obtain the interfacial interaction potential and the comparison of excess interfacial energy with Griffith's prediction for energy release rate is presented in the results section. Moreover, we quantify the role of P impurities on the TGB strength. Then the discussion section includes qualitative and quantitative analysis of the excess interfacial energy. Finally, we draw conclusions and summarize the work.

2. Computational methods

The atomistic MS simulations in this work were performed using the LAMMPS package [34,35]. To describe the interaction of the binary W-P system, we used the second nearest neighbor modified embedded atom method (2NN-MEAM [36,37]) potential developed in [38], because of its ability to capture P induced GB embrittlement. The potential also reproduces DFT prediction of fracture-relevant properties like the TS behavior and stacking fault energetics for different P impurity concentrations [38], which makes it suitable for the present study.

Table 1

Specifics of the $[1\bar{1}0]$ TGBs ($[1\bar{1}0]$ plane normal along y-axis, see Fig. 1) considered in the current work. The specified x-direction represents the crack propagation direction, whereas the z-direction is parallel to the crack front, see Fig. 1. Here, Φ is the GB twist angle in degrees. p and q are prime integer parameters such that $\Phi = 2\arctan(p/\sqrt{2}q)$ [39]. They are related to the Σ-parameter as $\Sigma = 2q^2 + p^2$ (whenever $2q^2 + p^2$ is odd) or $\Sigma = q^2 + p^2/2$ (if $2q^2 + p^2$ is even). The prime integers are also connected to the $y-$ and $z-$directions as $[\bar{p}, \bar{p}, 2q]$ and $[q, q, p]$, respectively.

| GB	x−direction	z−direction	Φ	p	q
$\Sigma 51$	$[\bar{1}\bar{1}10]$	$[551]$	$16.10°$	1	5
$\Sigma 33$	$[\bar{1}\bar{1}8]$	$[441]$	$20.05°$	1	4
$\Sigma 19$	$[\bar{1}\bar{1}6]$	$[331]$	$26.53°$	1	3
$\Sigma 27$	$[\bar{1}\bar{1}5]$	$[552]$	$31.59°$	2	5
$\Sigma 9$	$[\bar{1}\bar{1}4]$	$[221]$	$38.94°$	1	2
$\Sigma 11$	$[\bar{1}\bar{1}3]$	$[332]$	$50.48°$	2	3
$\Sigma 41$	$[\bar{3}\bar{3}8]$	$[443]$	$55.88°$	3	4
$\Sigma 3$	$[\bar{1}\bar{1}2]$	$[111]$	$70.53°$	1	1
$\Sigma 43$	$[\bar{3}\bar{3}5]$	$[556]$	$80.63°$	6	5
$\Sigma 17$	$[\bar{2}\bar{2}3]$	$[334]$	$86.63°$	4	3

Fig. 2. Distribution of P impurities at the $\Sigma 3$ TGB with impurity coverage $\theta = 0.06$ Å^{-2}. Here, '+' sign indicates the origin and W atoms are filtered out for better visibility of impurities.
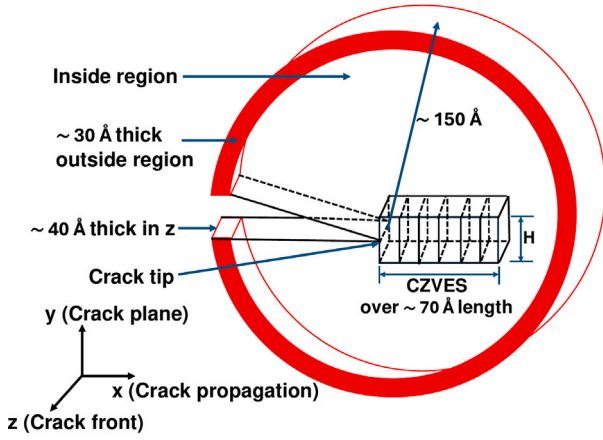
Fig. 1. Crack simulation setup in 3D.

2.1. Grain boundary geometries

The herein considered TGBs and their crystallographic orientations in relation to the crack setup, see Fig. 1, are listed in Table 1. It is emphasized that the amount of bond trapping observed for symmetric tilt GBs is generally highly dependent on the crack propagation direction [22,26,40], the way that the crack front directions were chosen for the current geometries, see Table 1, the two directions perpendicular to the crack front and crack plane are equivalent. Thus, TGB cracks do not exhibit such propagation directional anisotropy. For convenience, henceforth we drop the conventional notation for GBs and refer to them only by their Σ-value.

To produce the atomistic geometries we use the same strategy as outlined in our previous work [31]. Following this approach, the initial atomistic configurations of the pristine TGBs were generated using the open-source GB code [41]. By employing the γ-surface approach [4,6,42], the TGB geometries were brought to their ground state. Following this step – for impurity inhabited GBs – the P impurities were randomly introduced to resemble a narrow Gaussian density profile centered around the GB with a standard deviation of ~4 Å. Because P impurities preferentially segregate as substitutionals in the bulk [43], they were introduced by replacing W atoms in the GB proximity, such that it matched the target coverage, $\theta = 0.06$ Å^{-2}, which is defined as the number of impurity atoms per GB area unit. Under the assumption that all impurities segregate at the GBs, this impurity coverage would be equivalent to a P-impurity concentration of 10 wppm for a microstructure consisting of spherical grains with average diameter ~10 μm.
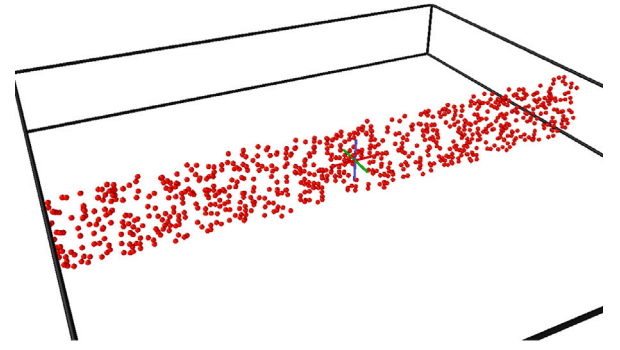
To update the positions of the randomly dispersed P impurity atoms to the equilibrium configuration, hybrid Monte Carlo (MC) and molecular dynamics (MD) simulations [44] were used. However, traditional MC simulations may exhibit lack of ergodicity whenever large atomic relaxations occur [45]. In the presence of impurities, this limitation tends to lead to high rejection rates for swapping impurity and host atoms, which can lead to artificial trapping at high energy sites [45]. In [31], it was observed that the P impurity atoms whose mobility in W is expected to be relatively low, were not segregated to the energetically favorable dislocation cores when GBs accommodated the dislocations. Therefore, the Metropolis algorithm [46–49] was used with a high temperature, $T = 2000$ K, which enabled a high acceptance rate for swapping the positions of W and P atoms during the MC part of the simulation. This approach ensured that in the presence of dislocations, the P atoms were quickly segregated to the energetically favorable dislocation cores [38]. The MD integration was conducted within the isobaric-isothermal (NPT) ensemble with the system temperature maintained at $T = 10$ K and the pressure kept at zero. The hybrid simulations with a timestep of 1 fs were carried out for a total time of 50 ps, which was sufficient for the atoms to relocate to equilibrium sites, see Fig. 2.

2.2. Extraction of excess interface energy

The adopted quasi-static MS fracture simulation setup for the TGB cracks studied herein is based on that previously presented in [31], see Fig. 1. It relies on a displacement-controlled mode-I loading and unloading scheme, with the displacement fields derived from anisotropic LEFM [26,50,51]. Here we only outline the necessary edits that were made to enable the extraction of interfacial excess properties. Instead, the reader is directed to [31] for a detailed account of the modeling setup.

Since the interfacial excess potential aims to relate the relaxed interplanar strain energy to the interplanar separation, a scheme that allows for the measurement of both is necessary. Moreover, it needs to account for variation associated with locally varying impurity concentration. To this end, the cohesive zone around the GB interface was subdivided into several CZVEs, see Fig. 1. Owing to the fact that all GBs underwent brittle failure, the fracture process zone is highly localized at the crack-tip. Thus, the CZVEs need to be chosen sufficiently small to capture the gradual cleavage energetics with high resolution. But because the bond strength varies within the GB structural unit, it must also be large enough so that any local variations can be averaged. Therefore the width was consistently chosen to be that of the GB structural unit, while the height of the CZVEs was chosen to be $H = 16$ Å. To avoid any spurious interactions between the crack tip atoms and the crack surfaces prior to loading, the first CZVE was placed at least 5.8 Å ahead of the crack tip. This distance corresponds to the interaction range of the potential.
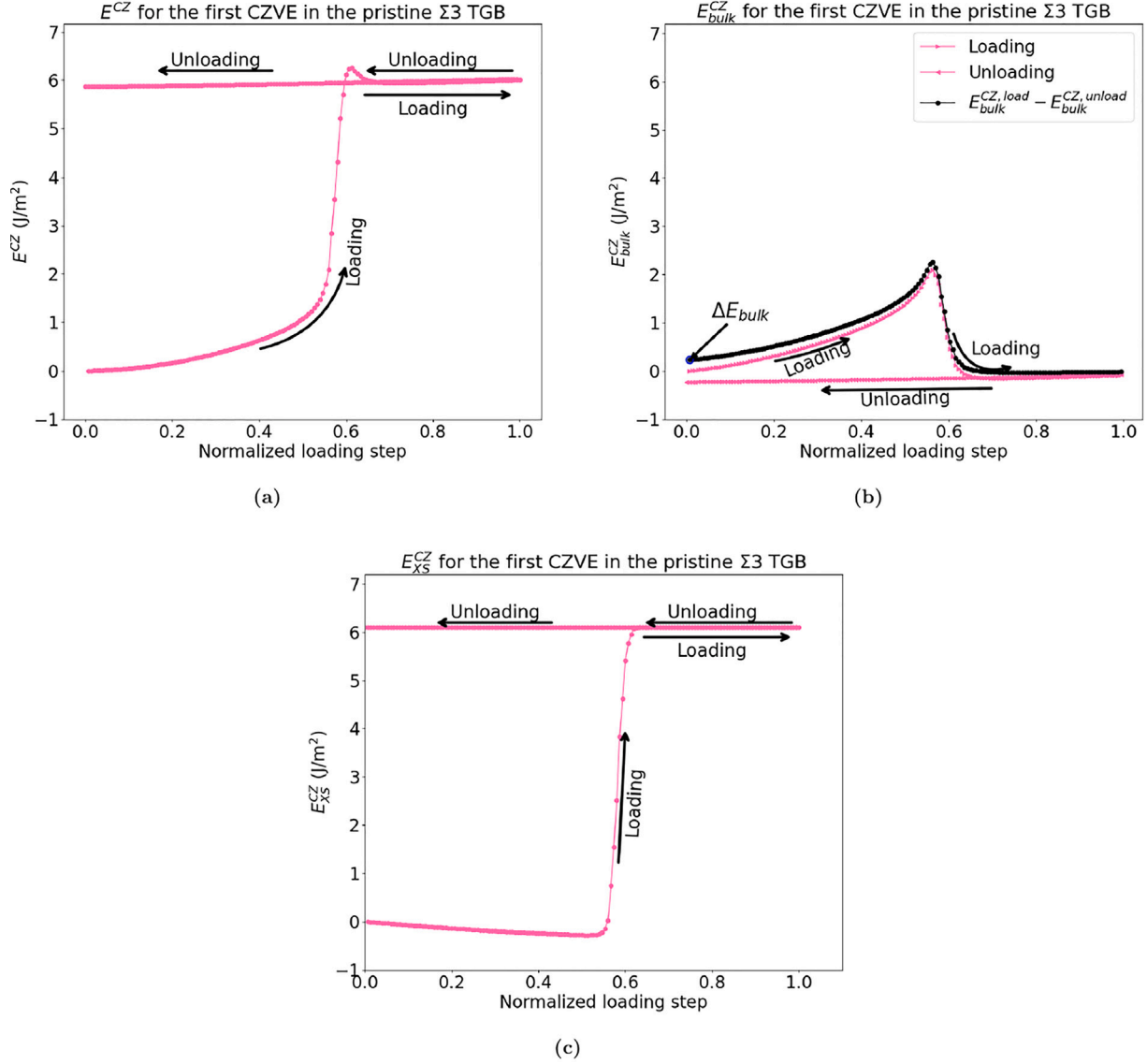
Fig. 3. (a) Plot of total potential energy E^{CZ} for the first CZVE vs. normalized loading step. (b) Evolution of E_{bulk}^{CZ} with normalized loading step. The black curve is obtained using $E_{bulk}^{CZ,load} - E_{bulk}^{CZ,unload}$. (c) Plot of E_{XS}^{CZ} vs. normalized loading step for the first CZVE. All the plots are for the pristine $\Sigma3$ TGB.

At every loading step, we first measured the total potential energy, E^{CZ}, stored in a CZVE due to the displacement fields, see Fig. 3(a). But because it scales with the CZVE volume, it was necessary to separate the strain energy into bulk and excess contributions. To achieve this, we first distinguished atoms at the low-coordinated surface from those in the bulk by using Voronoi tessellation as implemented in the Voro++ package [52]. This enabled us to identify the crack path and atoms of each CZVE that would end up above (top region) or below (bottom region) the fracture plane. Then we conducted a post-processing step where the strain energy of each relaxed configuration was recomputed, but with the interaction across the crack plane turned off, such that the bulk strain energy of each CZVE, E_{bulk}^{CZ}, could be computed (see Fig. 3(b)). This way the interfacial excess potential associated with the decohesion, E_{XS}^{CZ}, could be extracted using

$$E_{XS}^{CZ} = E^{CZ} - E_{bulk}^{CZ}, \tag{1}$$

which was evaluated for every loading and unloading step, see Fig. 3(c).

To identify the local separation, δ_{XS}^{CZ}, the Voronoi volumes of the cleavage surface atoms in each CZVE were summed to get the volume, V_i, enclosed by the surfaces at every loading instance i. The δ_{XS}^{CZ} was then computed as the area normalized change in V_i relative to the

reference pre-loading volume V_0, i.e. $(V_i - V_0)/A_{xz}$, where A_{xz} is the CZVE area projected on the crack plane. The E_{XS}^{CZ} was measured for all the CZVEs up to ~70 Å along the crack propagation direction and then fitted to an UBER-like function to get the average excess interface energy of the GB, denoted by E_{XS}. Henceforth, the "CZ" superscript is dropped whenever an average quantity of all CZVEs is considered.

2.3. Fitting of excess energy curves

To describe the energetics between two cleavage surfaces, Rose et al. [13] provided the so-called Rose's UBER. However, its functional format has previously had limited success when fitting to data that included surface relaxations [16,53–56]. Therefore, to describe the interaction between the relaxed cleavage planes, different extensions of the UBER were proposed [14,16,53–56]. However, since neither of those extensions did capture the cleavage energetics associated with the mode-I LEFM setup, some adjustments to enable fitting of the excess potential were needed.

As elaborated on in the Results section, the E_{XS}^{CZ} and E_{bulk}^{CZ} curves display some features that the UBER should capture. First, although the total strain energy (see Fig. 3(a)) increases during loading, E_{XS}^{CZ} exhibits

a local minimum during the initial loading phase (see Fig. 3(c)). This behavior was found for all GBs and CZVEs. To ensure that this was not an issue related to the used potential, additional test simulations using the embedded atom method potential by Ackland and Thetford [57] (henceforth referred to as AT-EAM) were performed. These simulations demonstrated the same features as found for the 2NN-MEAM potential, which indicates that they are not potential specific. Therefore, to describe $E_{XS}(\delta_{XS})$, it is imperative that not only the cleavage surface relaxations are considered, but also the local minimum. Accordingly, we propose the following relation

$$E_{XS}(\delta_{XS}) = -|E_b^0|\left(1 - \left(1 + \bar{\delta}_{XS}^m\right)\exp\left(-\bar{\delta}_{XS}^m\right)\right) + E^{min}\exp(-a\Delta) \quad (2)$$

where

$$\bar{\delta}_{XS}^m = \sum_{i=1}^{m}\left(\frac{\delta_{XS} - \delta_0}{\lambda_i}\right)^{2i-1}$$

and

$$\Delta = \left(\frac{\delta_{XS} - \delta_0}{\lambda_\Delta}\right)$$

The first term in Eq. (2) is identical to the extended UBER by Wilson et al. [53]. It comprises the binding energy term, E_b^0, the characteristic length parameters, λ_m ($m = 1, 2$), and δ_0, which is the local separation where the E_{XS} has its minimum. The binding energy term, E_b^0, equals the asymptotic energy of the E_{XS}^{CZ} curve (i.e. $E_b^0 = E_{XS}^{CZ}$ as $\delta_{XS}^{CZ} \to \infty$). The remaining parameters in Eq. (2), i.e. E_{min}, a and λ_Δ, are empirical fitting parameters that were introduced to capture the behavior of the E_{XS}-curves in the small displacement regime, i.e. δ_{XS} for which $E_{XS} < 0$.

Secondly, it is noticed that the initial energy level of E_{bulk}^{CZ} during loading and that following complete unloading do not match. This means that the strain energy in the bulk is not completely removed even after unloading, as illustrated by the black curve in Fig. 3(b), which represents the difference in bulk strain energy during loading and unloading. Therefore, an energy surplus corresponding to $\Delta E_{bulk} = E_{bulk}^{load,\delta_{XS}^{CZ}=0} - E_{bulk}^{unload,\delta_{XS}^{CZ}=0}$ is introduced into the interfacial excess potential during loading. Because the magnitude of ΔE_{bulk} is approximately the same amount by which the asymptotic limit of $E_{XS}(\delta_{XS} \to \infty)$ overestimates the theoretical ideal work of separation, W_{GB}^{sep}, a correction to Eq. (2) is needed. Consequently, it is multiplied by a scaling factor to diminish the overestimation of E_{XS}, i.e.,

$$E_{XS}^{scaled}(\delta_{XS}) = E_{XS}(\delta_{XS})\left[1 - \frac{\Delta E_{bulk}}{E_b^0}\right] \quad (3)$$

Eq. (3) is henceforth referred to as "xUBER", and differentiation respect to δ_{XS} yields the TS relationship given by

$$\sigma^{GB}(\delta_{XS}) = \left[-\frac{|E_b^0|}{\lambda_1}\left(-\bar{\delta}_{XS}^{m=2}\right)\exp\left(-\bar{\delta}_{XS}^{m=2}\right)\right.$$
$$-\frac{2|E_b^0|(\delta_{XS} - \delta_0)}{\lambda_2^2}\left(-\bar{\delta}_{XS}^{m=2}\right)\exp\left(-\bar{\delta}_{XS}^{m=2}\right)$$
$$\left.-\frac{aE^{min}\exp(-a\Delta)}{\lambda_3}\right] \times \left[1 - \frac{\Delta E_{bulk}}{E_b^0}\right]. \quad (4)$$

The traction, $\sigma^{GB}(\delta_{XS})$, has an inflection point at $\delta_{XS} = \delta_{crit}^{I,GB}$, which corresponds to the peak stress σ_{coh}^{GB}. To quantify the interaction range of the interfacial potential, we define $\delta_{max,sep}^{I,GB}$, which corresponds to the interplanar separation above which $\sigma^{GB}(\delta_{XS}) \leq 5$ MPa. Beyond this limit, two free surfaces are assumed to have formed as a result of the crack growth.

3. Results

3.1. Ideal grain boundary energy and work of separation

First and foremost, we determined the ground state configurations of a large set of $\langle 110 \rangle$ TGBs using the γ-surface approach. This enables
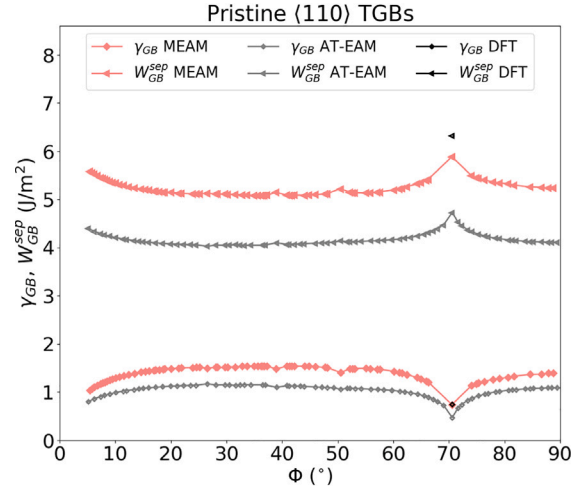

Fig. 4. Evaluated W_{sep}^{GB} and γ_{GB} curves of $\langle 110 \rangle$ TGBs for different twist angles. The red markers correspond to data for the 2NN-MEAM potential, while gray markers represent data for the AT-EAM potential from [58]. The γ_{GB} values for the AT-EAM potential are from Feng et al. [39] and the DFT data is from [4].

the computation of how the GB energy, γ_{GB}, varies with the twist angle, Φ, in the range of 0 to 90°, see Fig. 4. It is found that γ_{GB} for all the considered TGBs lies approximately between 0.74 and 1.55 J/m², with $\Sigma 3$ being the lowest energy TGB with $\Phi = 70.53°$. The GB energy of the $\Sigma 3$ TGB predicted herein is in very good agreement with the DFT study by Scheiber et al. [4]. Notably, Feng et al. [39] studied energies of several $\langle 110 \rangle$ TGBs using the EAM potential by Juslin and Wirth [58]. This potential relies on the AT-EAM potential [57] with a slightly adjusted core-repulsion to describe the W-W interaction. A comparison of the herein computed γ_{GB} profile with that in [39] shows that both yield similar profiles for varying Φ, see Fig. 4. But notably the prediction in [39] is consistently low. Since the anticipated cleavage surfaces for these GBs correspond to {110}-type, for which the relaxed surface energy $\gamma_{\{110\}} = 3.38$ J/m² for the utilized 2NN-MEAM potential [26], the ideal work of separation can readily be approximated as $W_{GB}^{sep} = 2\gamma_{\{110\}} - \gamma_{GB}$. It is found to lie in the range between 5.08 and 5.89 J/m² for all the TGBs, see Fig. 4. The upper limit of this data occurs for the $\Sigma 3$ GB, for which DFT has predicted the ideal work of separation to be 6.32 J/m² [4]. Consistent with the low γ_{GB}, the use of the AT-EAM potential leads to ideal work of separation for all the TGBs lower than those computed herein, with similar profiles for varying Φ, see Fig. 4. The AT-EAM potential predicts W_{GB}^{sep} for $\Sigma 3$ TGB ~ 1.6 J/m² lower than that by DFT. Thus, the estimates of the utilized 2NN-MEAM potential are in good agreement with DFT and an improvement compared to the AT-EAM potential. This is indicative of the good predictive strength of the herein utilized 2NN-MEAM potential [38].

3.2. Grain boundary crack behavior

The cracks in all the pristine $\langle 110 \rangle$ TGBs considered in this work, see Table 1, underwent brittle crack propagation under mode-I K_I-controlled loading. In light of {110}-type surfaces being the most densely packed in BCC crystals with the lowest surface energy [4,26], as expected, brittle failure occurred at the GB interface and then propagated on the {110}-cleavage plane, see Fig. 5(a). Segregation of P impurities did not affect the mode of failure, which remained to be brittle cleavage for all GBs. However, occasionally the post-fracture cleavage planes were irregular, with the formation of debris of clustered W-P agglomerates of thickness approximately equal to one to two atom layers. They were typically decorated with P-impurities and formed when a set of locally dispersed P-atoms weakened the cohesion of a
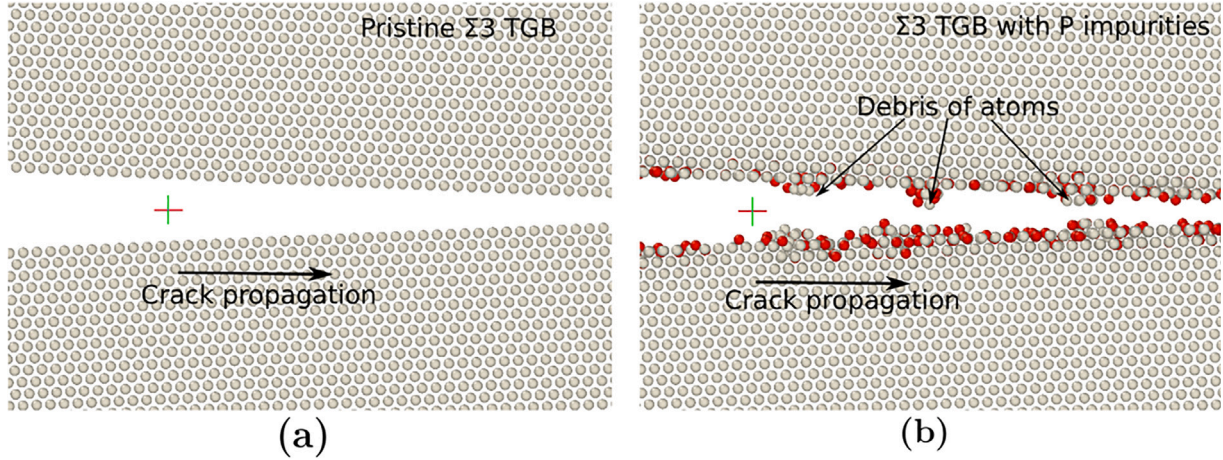
Fig. 5. Simulation snapshots of crack tip behavior in $\Sigma 3$ TGB for (a) $\theta = 0.0$ Å^{-2} and (b) $\theta = 0.06$ Å^{-2}. Here, '+' indicates the original crack tip.

layer parallel to the GB interface, onto which the crack propagated, see Fig. 5(b). Such fracture mechanisms tend to yield increased energy release rate [31].

3.3. Interfacial excess potential and xUBER

The data pairs $(\delta_{XS}^{CZ}, E_{XS}^{CZ})$ for individual CZVEs from the K_I- loading simulations of the TGBs are fitted to Eq. (2) and the scaled xUBER in Eq. (3) to procure interfacial excess potential profiles. The optimized parameters for all the TGBs are also made available in Table 2. For example, the fitted data for pristine and P inhabited $\Sigma 3$ TGB cracks are presented in Fig. 6, while the remaining curves are available in the supplementary material in Figures S1–S9. In Fig. 6(a), the $E_{XS}^{CZ}(\delta_{XS}^{CZ})$ curves of different CZVEs overlap for the pristine $\Sigma 3$ TGB. The same observation was made for the remaining pristine TGBs (see Figures S1–S9 in the supplementary material). This indicates that the E_{XS}^{CZ} is independent of the position of CZVEs relative to the initial crack tip. In these figures, the orange curve corresponds to the fit to Eq. (2) and the green curve represents the corrected xUBER (i.e. the curve of Eq. (3)).

The root mean squared error (RMSE) of the fits to Eq. (2) are small for pristine TGB data. The maximum RMSE is $\sim$0.15 J/m^2. However, the RMSE of the impurity inhabited TGBs are larger than those of the pristine TGB data, with the largest RMSE being $\sim$0.23 J/m^2. The increased RMSE in the latter case is due to the scattering of the $(\delta_{XS}^{CZ}, E_{XS}^{CZ})$ data, as shown in Fig. 6(b). It is caused by the locally varying P impurity coverage and the proximity of P segregation sites relative to the crack plane, which influence the local cohesion. In [31] the same factors were reported to affect the energy release rate (and thereby the local fracture toughness) associated with crack propagation in individual CZVEs of symmetric tilt GBs. These variations give rise to different fracture mechanisms, including impurity-induced deflection of the crack onto planes with higher energy release rate, which sometimes yields locally higher fracture toughness, as reported in [31]. The scaled xUBER is different from that in Eq. (2) only by the scaling factor $1 - \Delta E_{bulk}/E_b^0$, which can be readily extracted from the simulations. This adjustment enables the formulation of an excess potential that reproduces the accurate energy release rate, and provides a good estimate of the TS behavior leading up to complete cleavage.

The asymptotic limit of E_{XS}^{scaled} is equal to the interfacial binding energy of the crack surfaces, $E_b^{0,scaled}$, which corresponds to $E_b^0 - \Delta E_{bulk}$ (see Table 2). For all the pristine TGB cracks, it is found to be comparable with the corresponding ideal work of separation, see Fig. 7. The highest value is seen for the $\Sigma 3$ TGB implying a higher energy requirement for a crack to propagate. This is in line with the lowest

Table 2

Optimized xUBER (Eq. (3)) and TS law (Eq. (4)) parameters for all TGBs. Here, E_b^0, E^{min} and ΔE_{bulk} are all in units of J/m^2, whereas the length parameters λ_1, λ_2, λ_Δ and δ_0 have the unit Å. The fitting parameter a is dimensionless.

GB	θ	E_b^0	E^{min}	ΔE_{bulk}	a	λ_1	λ_2	λ_Δ	δ_0
$\Sigma 51$	0.0	5.726	−0.199	0.529	0.7076	0.8757	3.9918	0.603	0.211
	0.06	5.2518	−0.2417	0.9545	0.9804	0.7808	3.5013	0.7338	0.2326
$\Sigma 33$	0.0	5.676	−0.1938	0.5204	0.3910	0.8256	3.3309	0.2990	0.2162
	0.06	5.6207	−0.2061	0.9634	0.9973	0.9617	2.685	0.5861	0.2733
$\Sigma 19$	0.0	5.6533	−0.2050	0.5141	0.9666	0.7941	2.9659	0.6242	0.2364
	0.06	5.6048	−0.2501	0.9634	0.9292	0.7394	3.2530	0.5247	0.2553
$\Sigma 27$	0.0	5.6409	−0.2529	0.4160	0.9624	0.7503	3.0196	0.7474	0.2511
	0.06	5.8553	−0.2448	1.0511	0.9408	0.9235	3.4035	0.6183	0.2836
$\Sigma 9$	0.0	5.600	−0.2012	0.4439	0.7612	0.6258	1.6582	0.1549	0.3114
	0.06	5.6766	−0.3458	1.0613	0.9675	0.7872	2.0488	0.5267	0.3317
$\Sigma 11$	0.0	5.6039	−0.2178	0.3524	0.8933	0.7073	1.8652	0.2488	0.3062
	0.06	5.3189	−0.2213	0.7502	0.4907	0.7655	1.9732	0.2563	0.2617
$\Sigma 41$	0.0	5.540	−0.1797	0.3944	0.8381	0.8817	3.8696	0.6581	0.2145
	0.06	5.148	−0.1411	0.9186	0.8792	0.8644	3.4705	0.5491	0.1774
$\Sigma 3$	0.0	6.099	−0.2823	0.1858	0.4651	0.7329	2.0217	0.1737	0.3092
	0.06	5.8439	−0.3466	0.6106	0.6515	0.8574	1.9343	0.3775	0.3556
$\Sigma 43$	0.0	5.9458	−0.2286	0.599	0.8682	0.8331	4.7154	0.6808	0.2334
	0.06	5.9222	−0.2806	1.514	0.8777	0.9965	3.6567	0.7435	0.2692
$\Sigma 17$	0.0	5.9139	−0.2392	0.6506	0.6855	0.7712	2.3081	0.4038	0.2546
	0.06	6.1269	−0.3100	1.273	0.996	0.8905	2.5058	0.5386	0.3356

γ_{GB} observed for this specific TGB. The maximum observed deviation of the binding energy from W_{GB}^{sep}, though minuscule ($\sim$2.4%), is for $\Sigma 27$. For all the remaining pristine TGB cracks, the deviation is less than 0.5%. As anticipated, the P impurities segregated at the TGBs reduce the binding energy, while the amount of reduction varies for different TGBs, see Fig. 7.

3.4. Traction separation behavior

The $(\delta_{XS}^{CZ}, E_{XS}^{CZ})$ data and xUBER are CZVE height independent because the bulk strain energy is removed, such that it represents the local interfacial energy associated with the gradual separation of two adjacent planes. Accordingly, the TS behavior obtained from xUBER is also scale-independent. Using the fitting parameters provided in Table 2 in Eq. (4) for the respective TGB cracks, the TS behavior of the cleavage surfaces is obtained, see Fig. 8 for the $\Sigma 3$ GB. The profile of TS curves resemble the typical positively skewed bell-shaped TS behavior, see Fig. 8, as observed in DFT [26]. The TS curves for the remaining TGBs exhibit the same type of behavior. They are provided in the supplementary material in Figures S10–S18.
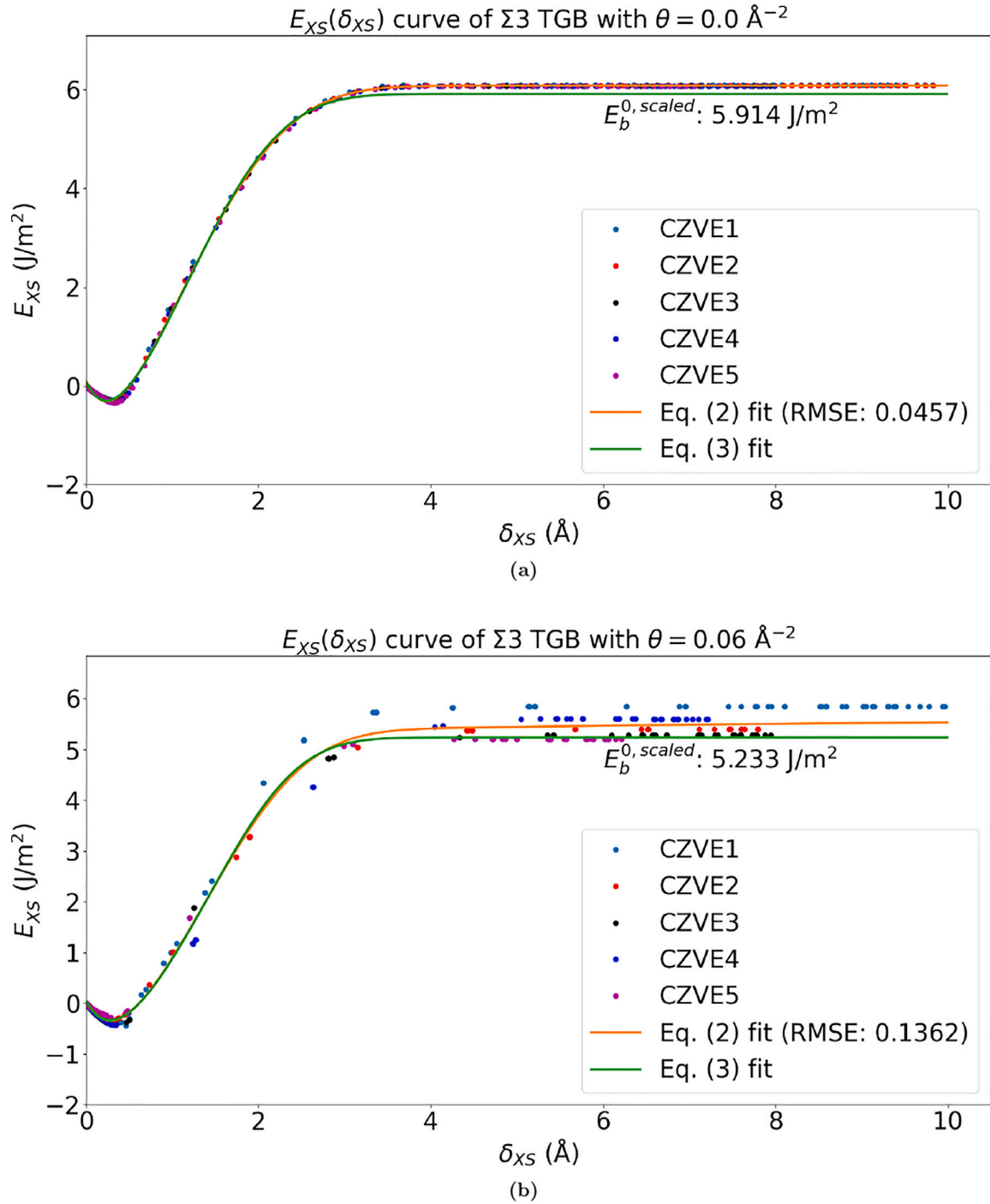
Fig. 6. Excess interface energetics ($E_{XS}(\delta_{XS})$–curve) for (a) pristine and (b) $\theta = 0.06$ Å^{-2} Σ3 TGB. The $E_{XS}(\delta_{XS})$–curves for the remaining TGBs are provided in the supplementary material. The different markers correspond to different CZVEs (CZVE1-CZVE5) located at varying distances from the initial crack tip.

Based on the peak stresses, σ_{coh}^{GB}, extracted from the TS curves for pristine TGB cracks, Σ9, Σ3 and Σ11, in order, with peak stresses of 38.3 GPa, 36.3 GPa and 34.4 GPa, respectively, are found to be the strongest, see Fig. 9. The Σ51 and Σ41 are the weakest of the considered pristine TGBs. The peak stress generally reduces upon the introduction of impurities. It is seen, however, that its reduction varies considerably among the TGBs. For example, the Σ9 TGB shows the maximum decrease, of ~11.7 GPa, in σ_{coh}^{GB}, whereas Σ51 and Σ19 are the least affected TGBs as a minimum reduction of ~1.85 GPa is observed for the GBs. On average, the reduction of the peak stress is ~5.4 GPa. Concerning the impact of impurities on the location of the inflection

point and the excess potential interaction range, no clear trends could be seen for how P impurities affect $\delta_{crit}^{I,GB}$ and $\delta_{max,sep}^{I,GB}$.

4. Discussion

All the ⟨110⟩ TGBs share the same surfaces constituting the interfaces. The differences in the TGBs arise from the varying number of coincidence lattice sites, which is related to their Σ-values [59]. Accordingly, as expected, the range of both γ_{GB} and W_{GB}^{sep} for all the ⟨110⟩ TGBs is very narrow, with the difference between the maximum and minimum values being ~0.8 J/m^2.

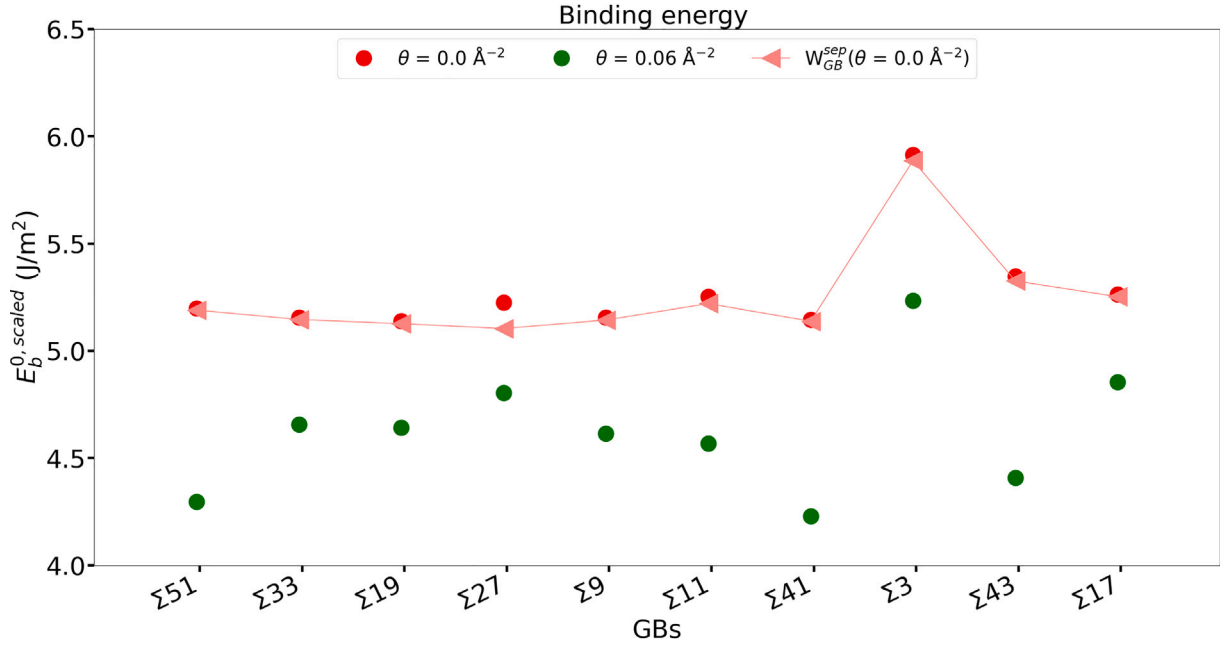**Fig. 7.** The $E_b^{0,scaled}$ vs. TGBs curves for P impurity coverage, $\theta = 0.0$ Å^{-2} and $= 0.06$ Å^{-2}. The raw data for this plot is available in the supplementary material.

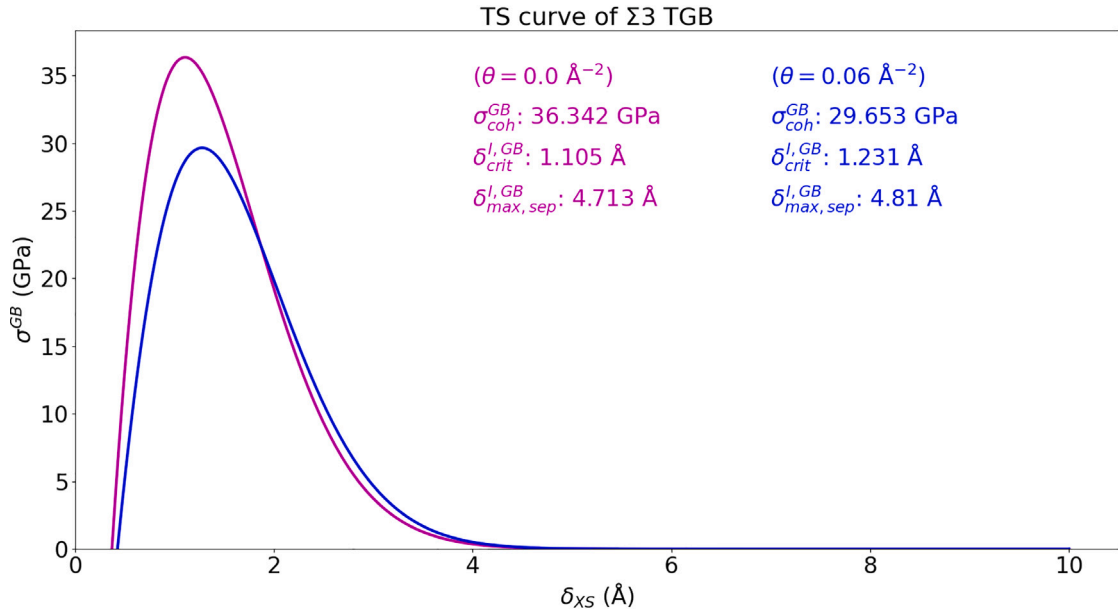**Fig. 8.** TS curve of $\Sigma3$ TGB with $\theta = 0.0$ Å^{-2} (purple) and $\theta = 0.06$ Å^{-2} (blue). The TS curves for the remaining TGBs are provided in the supplementary material.

As for the crack path, the observed brittle growth of pristine TGB cracks occurs along the {110} since those surfaces exhibit the lowest surface energy for W [26]. Even though there is a small variation in γ_{GB} for the considered GBs, it is not sufficient to activate any alternative crack paths in the pristine case. The impurity inhabited GB cracks also exhibit growth along the interface. However, the fractured {110} surfaces are typically decorated with P impurities and covered locally with debris of W-P clusters, which shows that the fracture is not as clean as in the pristine case and that deviations from the original crack plane emerge locally.

When using K_I-controlled displacement loading, a truly uniaxial loading is achieved only at the crack tip. Therefore, the origin from which the displacements are computed needs to be updated as the crack advances to maintain the uniaxial state throughout the simulation. But – as alluded to in the introduction – there are numerical challenges

connected to uniquely locating the crack-tip of an advancing crack. This becomes apparent in the presence of impurities that may cause the crack front to deviate from a straight line [31]. For this reason, we opted not to do that in the present work. However, despite this simplification, somewhat surprisingly the interfacial excess potential curves were found to be identical in all the CZVEs of the pristine TGBs – regardless of their position relative to the initial crack tip location – see e.g. Fig. 6(a). We believe that this is due to the interfacial excess being independent of the bulk strain energy, and that any in-plane stress contributions to the strain energy are negligible compared to that of the normal traction as the material fractures. This is indicative of E_{XS}^{CZ} being independent of whether the origin of the displacement fields is updated or not. Consequently, E_{XS}^{CZ} should be a good approximation to describe the TS behavior of P segregated GB cracks too.
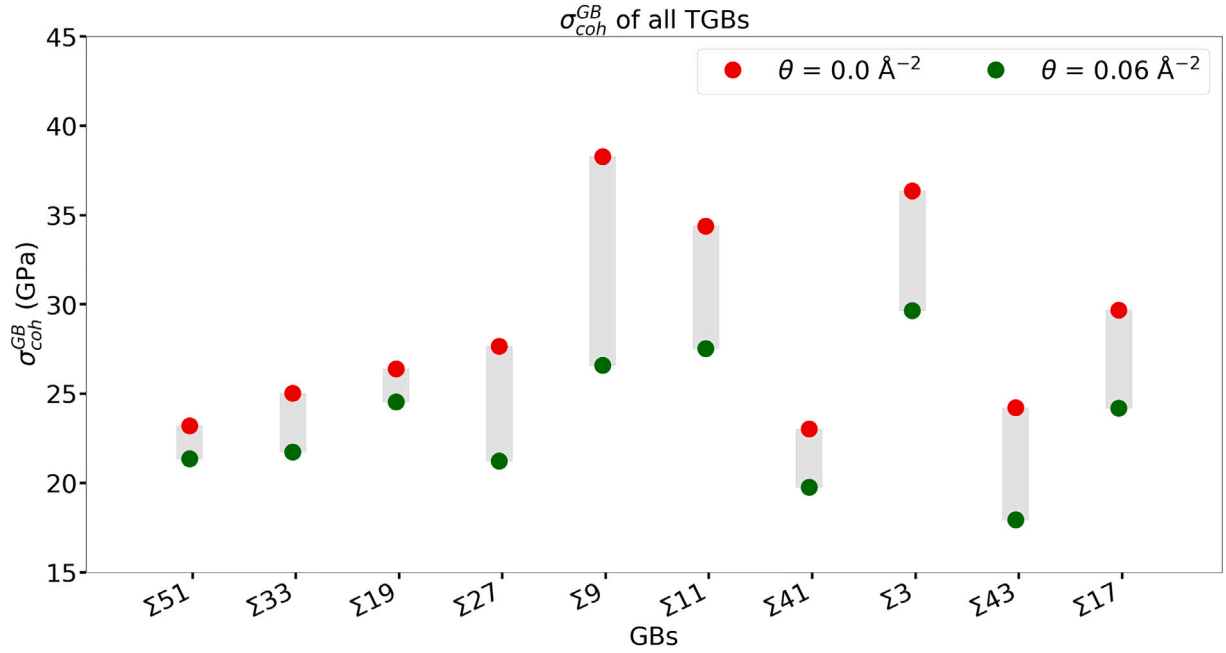
Fig. 9. The σ_{coh}^{GB} vs. TGBs curve for P impurity coverage, $\theta = 0.0$ Å^{-2} and $= 0.06$ Å^{-2}. The raw data for this plot is available in the supplementary material.

An observed feature that requires some elaboration is the parabolic region around the minimum in the interfacial excess curves. Such behavior does not emerge whenever bonds between atoms of two adjacent and parallel decohering planes are uniformly stretched, as is the case for instance in tensile simulations, see e.g. [10–12,14–16,19–21,38,56]. However, the loading of an atomically sharp crack brings about stress build-up at the crack tip. As a consequence of this, the crack tip profile undergoes changes in its curvature leading to cusp-like crack tip. This process is associated with an increase in bulk strain energy, as shown in Fig. 3(b), leading to the minimum in the interfacial excess curves, Figs. 3(c) and 6, via Eq. (1). Following the crack propagation, the built-up stress reduces along with the release of bulk strain energy (thereby increasing E_{XS}) through the creation of traction free surfaces. Thus, we believe that the stress state at the crack tip is responsible for the region around the minimum in Figs. 3(c) and 6. Although we do not intend to investigate it further here, we note that the induced stress state in the fracture process zone ahead of such cusp-like crack tips has been successfully described using strain gradient elasticity theory, see e.g. Kotoul et al. [60].

The parabolic region around the minimum in the interfacial excess curves is not captured by Rose's UBER and its extensions available in the literature [14,16,53–56]. Therefore, to enable capturing of the energetics, including the local energy minimum, associated with the crack surface formation in our simulations, the term $E^{min}\exp(-a\Delta)$ is added to the extension to the UBER proposed by Wilson et al. [53]. This results in Eqs. (2) and (3). However, we note that this correction gives rise to a TS relation with negative traction for low δ_{XS}. To implement such TS relation, for instance, in the finite element method, it would be beneficial to adjust the curves by setting $E^{min} = 0$, which would remove the initial negative traction. Because the $E^{min}-$ values lie in the approximate range of 0.14–0.35 J/m^2, this would yield a change of the binding energy corresponding to only ~6 %, see Table 2, which may be an acceptable approximation — depending on the application. Moreover, one could assign $\delta_0 = 0$, which would shift the curve such that $\delta_{XS} = 0$ corresponds to the minimum of the TS curve. Thus by setting (E^{min}, δ_{XS}) as the origin, there would be less variation in energy gradient and the TS behavior would better resemble existing TS laws for cohesive zone modeling, see e.g. [61].

Another observation from the crack simulations is the bulk strain energy dissipation post loading and unloading of the system. The bulk

strain energy steadily rises with the loading, and upon crack propagation initiation, the E_{bulk} starts to fall rapidly until traction-free surfaces are formed, see Fig. 3(b). Unloading from this state shows that E_{bulk} does not traverse the loading path back to zero, thus implying that extra energy was introduced into the E_{XS} of the system, via Eq. (1), during loading, see Fig. 3(b). Because the E_{XS} curve in Fig. 3(c) is constant during unloading, the source for this extra energy is the relaxation of the strain in bulk. As previously mentioned, this extra energy needs to be taken into account to obtain the excess potential. The proposed xUBER (Eq. (3)), does precisely that by rescaling E_{XS} using ΔE_{bulk} and thereby lowering it for the entire range of separation.

The advantage of adopting the loading and unloading scheme outlined in the present work is that the necessary data points can be readily extracted and the scaling factor emerges naturally from the strain energy difference between the loading and unloading curves at zero strain. This is beneficial, especially in the case of impurity inhabited GBs, where the cleavage plane may vary locally and the overestimation of the interfacial excess potential cannot be easily assessed. Moreover, the approach does not constrain the crack to follow a prescribed fracture plane, instead, it is free to propagate onto adjacent planes or form atomic clusters on the fracture surface if energetically preferable. In the event of randomly dispersed impurities, this produces a more realistic crack surface than if the crack was constrained to a predefined plane.

5. Summary and conclusions

In this study, we have designed a procedure to estimate the interfacial excess potential associated with cleavage of pristine and impurity inhabited ⟨110⟩ TGB cracks. The TGB cracks were loaded using mode-I K_I-controlled displacement fields in a quasi-static MS setting and the strain energy and interplanar separation were measured using CZVEs along the crack path.

An xUBER is proposed for the crack simulation data and the parameterization shows that the data is fitted satisfactorily to the xUBER. The decohesion process is local and involves only the local separation of the adjacent planes. Therefore the approach adopted here to extract excess potential data is scale-independent.

From the parameterization, it can be inferred that the xUBER well describes the decohesion energetics during the brittle growth of a

crack. Further, the TS behavior based on the xUBER captures the anticipated traits of an atomistically-informed TS law, i.e. it produces a positively skewed bell-shaped curve. The observed trend in excess potential and TS peak stress under the influence of P impurities concurs with experimental P induced GB embrittlement in W GBs. Therefore, we believe that the approach presented here can be applied to other types of W GBs in their pristine or impurity inhabited form.

CRediT authorship contribution statement

Praveenkumar Hiremath: Writing – review & editing, Writing – original draft, Methodology, Investigation, Formal analysis, Conceptualization. **Solveig Melin:** Writing – review & editing, Supervision, Funding acquisition. **Pär A.T. Olsson:** Writing – review & editing, Supervision, Methodology, Funding acquisition, Conceptualization.

Declaration of competing interest

The authors declare that they have no known competing financial interests or personal relationships that could have appeared to influence the work reported in this paper.

Acknowledgments

Appendix A. Supplementary data

Supplementary material related to this article can be found online at https://doi.org/10.1016/j.commatsci.2025.113722.

Data availability

The data required to reproduce these findings is available in the supplementary material.

References

[1] D. Lee, Fracture of drawn tungsten wires, Met. Trans. A 6 (1975) 2083–2088.

[2] C. Ren, Z.Z. Fang, M. Koopman, B. Butler, J. Paramore, S. Middlemas, Methods for improving ductility of tungsten-a review, Int. J. Refract. Met. Hard Mater. 75 (2018) 170–183.

[3] B. Gludovatz, S. Wurster, T. Weingärtner, A. Hoffmann, R. Pippan, Influence of impurities on the fracture behaviour of tungsten, Phil. Mag. 91 (22) (2011) 3006–3020.

[4] D. Scheiber, R. Pippan, P. Puschnig, L. Romaner, Ab initio calculations of grain boundaries in bcc metals, Modelling Simul. Mater. Sci. Eng. 24 (3) (2016) 035013.

[5] A. Joshi, D. Stein, Intergranular brittleness studies in tungsten using auger spectroscopy, Met. Trans. 1 (1970) 2543–2546.

[6] W. Setyawan, R.J. Kurtz, Effects of transition metals on the grain boundary cohesion in tungsten, Scr. Mater. 66 (8) (2012) 558–561.

[7] S. Dorfman, V. Liubich, D. Fuks, K.C. Mundim, Simulations of decohesion and slip of the $\Sigma 3\langle 111\rangle$ grain boundary in tungsten with non-empirically derived interatomic potentials: the influence of boron interstitials, J. Phys.: Condens. Matter. 13 (31) (2001) 6719.

[8] A. Giannattasio, Z. Yao, E. Tarleton, S. Roberts, Brittle–ductile transitions in polycrystalline tungsten, Phil. Mag. 90 (30) (2010) 3947–3959.

[9] O. Nguyen, M. Ortiz, Coarse-graining and renormalization of atomistic binding relations and universal macroscopic cohesive behavior, J. Mech. Phys. Solids 50 (8) (2002) 1727–1741.

[10] P.A.T. Olsson, K. Kese, M. Kroon, A.M. Alvarez Holston, Ab initio-based fracture toughness estimates and transgranular traction-separation modelling of zirconium hydrides, Modelling Simul. Mater. Sci. Eng. 23 (4) (2015) 045015.

[11] P.A.T. Olsson, M. Mrovec, M. Kroon, First principles characterisation of brittle transgranular fracture of titanium hydrides, Acta Mater. 118 (2016) 362–373.

[12] A. Van der Ven, G. Ceder, The thermodynamics of decohesion, Acta Mater. 52 (5) (2004) 1223–1235.

[13] J.H. Rose, J.R. Smith, J. Ferrante, Universal features of bonding in metals, Phys. Rev. B 28 (4) (1983) 1835.

[14] P.A.T. Olsson, J. Blomqvist, Intergranular fracture of tungsten containing phosphorus impurities: A first principles investigation, Comput. Mater. Sci. 139 (2017) 368–378.

[15] A.A. Guzmán, J. Jeon, A. Hartmaier, R. Janisch, Hydrogen embrittlement at cleavage planes and grain boundaries in bcc iron—revisiting the first-principles cohesive zone model, Materials 13 (24) (2020) 5785.

[16] E. Toijer, P.A.T. Olsson, P. Olsson, Ab initio modelling of intergranular fracture of nickel containing phosphorus: Interfacial excess properties, Nucl. Mater. Energy 28 (2021) 101055.

[17] A.W. Thompson, I.M. Bernstein, Effect of Hydrogen on Behavior of Materials, Tech. Rep, Metallurgical Society of AIME, New York, 1976.

[18] J.R. Rice, J.-S. Wang, Embrittlement of interfaces by solute segregation, Mater. Sci. Eng. A 107 (1989) 23–40.

[19] D.E. Spearot, K.I. Jacob, D.L. McDowell, Non-local separation constitutive laws for interfaces and their relation to nanoscale simulations, Mech. Mater. 36 (9) (2004) 825–847.

[20] V. Yamakov, E. Saether, E. Glaessgen, Multiscale modeling of intergranular fracture in aluminum: constitutive relation for interface debonding, J. Mater. Sci. 43 (2008) 7488–7494.

[21] W. Barrows, R. Dingreville, D. Spearot, Traction–separation relationships for hydrogen induced grain boundary embrittlement in nickel via molecular dynamics simulations, Mater. Sci. Eng. A 650 (2016) 354–364.

[22] J.J. Möller, E. Bitzek, Fracture toughness and bond trapping of grain boundary cracks, Acta Mater. 73 (2014) 1–11.

[23] J.J. Möller, Atomistic Simulations of Crack Front Curvature Effects and Crack-Microstructure Interactions (Ph.D. thesis), Friedrich - Alexander - Universität Erlangen - Nürnberg, 2017.

[24] J.J. Möller, E. Bitzek, R. Janisch, H. ul Hassan, A. Hartmaier, Fracture ab initio: A force-based scaling law for atomistically informed continuum models, J. Mater. Res. 33 (22) (2018) 3750–3761.

[25] P. Andric, W. Curtin, New theory for Mode I crack-tip dislocation emission, J. Mech. Phys. Solids 106 (2017) 315–337.

[26] P. Hiremath, S. Melin, E. Bitzek, P.A.T. Olsson, Effects of interatomic potential on fracture behaviour in single-and bicrystalline tungsten, Comput. Mater. Sci. 207 (2022) 111283.

[27] M. Grujicic, H. Zhao, G. Krasko, Atomistic simulation of $\Sigma 3$ (111) grain boundary fracture in tungsten containing various impurities, Int. J. Refract. Met. Hard Mater. 15 (5–6) (1997) 341–355.

[28] W.-S. Ko, N.J. Kim, B.-J. Lee, Atomistic modeling of an impurity element and a metal–impurity system: pure P and Fe-P system, J. Phys.: Condens. Matter. 24 (22) (2012) 225002.

[29] W.A. Curtin, On lattice trapping of cracks, J. Mater. Res. 5 (7) (1990) 1549–1560.

[30] P. Andric, W.A. Curtin, Atomistic modeling of fracture, Modelling Simul. Mater. Sci. Eng. 27 (1) (2018) 013001.

[31] P. Hiremath, S. Melin, P.A.T. Olsson, Phosphorus driven embrittlement and atomistic crack behavior in tungsten grain boundaries, Comput. Mater. Sci. 244 (2024) 113194.

[32] D. Tanguy, Cohesive stress heterogeneities and the transition from intrinsic ductility to brittleness, Phys. Rev. B 96 (17) (2017) 174115.

[33] D. Tanguy, Constrained molecular dynamics for quantifying intrinsic ductility versus brittleness, Phys. Rev. B— Condens. Matter Mater. Phys. 76 (14) (2007) 144115.

[34] S. Plimpton, Fast parallel algorithms for short-range molecular dynamics, J. Comput. Phys. 117 (1) (1995) 1–19.

[35] A.P. Thompson, H.M. Aktulga, R. Berger, D.S. Bolintineanu, W.M. Brown, P.S. Crozier, P.J. in 't Veld, A. Kohlmeyer, S.G. Moore, T.D. Nguyen, R. Shan, M.J. Stevens, J. Tranchida, C. Trott, S.J. Plimpton, LAMMPS - a flexible simulation tool for particle-based materials modeling at the atomic, meso, and continuum scales, Comput. Phys. Comm. 271 (2022) 108171.

[36] B.-J. Lee, M.I. Baskes, Second nearest-neighbor modified embedded-atom-method potential, Phys. Rev. B 62 (2000) 8564–8567.

[37] B.-J. Lee, M. Baskes, H. Kim, Y. Koo Cho, Second nearest-neighbor modified embedded atom method potentials for bcc transition metals, Phys. Rev. B 64 (2001) 184102.

[38] P.A.T. Olsson, P. Hiremath, S. Melin, Atomistic investigation of the impact of phosphorus impurities on the tungsten grain boundary decohesion, Comput. Mater. Sci. 219 (2023) 112017.

[39] Y.-X. Feng, J.-X. Shang, Z.-H. Liu, G.-H. Lu, The energy and structure of (110) twist grain boundary in tungsten, Appl. Surf. Sci. 357 (2015) 262–267.

[40] P. Gumbsch, Brittle fracture and the brittle-to-ductile transition of tungsten, J. Nucl. Mater. 323 (2–3) (2003) 304–312.

[41] R. Hadian, B. Grabowski, J. Neugebauer, GBcode: A grain boundary generation code, J. Open Source Softw. 3 (29) (2018) 900.

[42] D. Terentyev, X. He, A. Serra, J. Kuriplach, Structure and strength of ⟨110⟩ tilt grain boundaries in bcc Fe: An atomistic study, Comput. Mater. Sci. 49 (2) (2010) 419–429.

[43] D. Scheiber, R. Pippan, P. Puschnig, L. Romaner, Ab initio search for cohesion-enhancing impurity elements at grain boundaries in molybdenum and tungsten, Modelling Simul. Mater. Sci. Eng. 24 (8) (2016) 085009.

[44] B. Sadigh, P. Erhart, A. Stukowski, A. Caro, E. Martinez, L. Zepeda-Ruiz, Scalable parallel Monte Carlo algorithm for atomistic simulations of precipitation in alloys, Phys. Rev. B 85 (18) (2012) 184203.

[45] D. Tanguy, Sampling vacancy configurations with large relaxations using smart darting, Phys. Rev. Mater. 8 (3) (2024) 033604.

[46] N. Metropolis, A.W. Rosenbluth, M.N. Rosenbluth, A.H. Teller, E. Teller, Equation of state calculations by fast computing machines, J. Chem. Phys. 21 (6) (1953) 1087–1092.

[47] G. Bhanot, The metropolis algorithm, Rep. Progr. Phys. 51 (3) (1988) 429.

[48] P. Diaconis, L. Saloff-Coste, What do we know about the Metropolis algorithm? J. Comput. System Sci. 57 (1) (1998) 20–36.

[49] I. Beichl, F. Sullivan, The metropolis algorithm, Comput. Sci. Eng. 2 (1) (2000) 65–69.

[50] G.C. Sih, P. Paris, G. Irwin, On cracks in rectilinearly anisotropic bodies, Int. J. Fract. Mech. 1 (3) (1965) 189–203.

[51] G.C. Sih, H. Liebowitz, Mathematical theories of brittle fracture, in: H. Liebowitz (Ed.), Fracture: An Advanced Treatise, in: Mathematical Fundamentals, Vol. 2, Academic Press, NY, 1968, pp. 67–190.

[52] C.H. Rycroft, VORO++: A three-dimensional Voronoi cell library in C++, Chaos (ISSN: 1054-1500) 19 (4) (2009) 041111.

[53] B.T. Wilson, J.D. Robson, P. Shanthraj, C.P. Race, Simulating intergranular hydrogen enhanced decohesion in aluminium using density functional theory, Modelling Simul. Mater. Sci. Eng. 30 (3) (2022) 035009.

[54] R.L. Hayes, M. Ortiz, E.A. Carter, Universal binding-energy relation for crystals that accounts for surface relaxation, Phys. Rev. B 69 (17) (2004) 172104.

[55] A. Srirangarajan, A. Datta, A.N. Gandi, U. Ramamurty, U.V. Waghmare, Universal binding energy relation for cleaved and structurally relaxed surfaces, J. Phys.: Condens. Matter. 26 (5) (2013) 055006.

[56] R.A. Enrique, A. Van der Ven, Traction curves for the decohesion of covalent crystals, Appl. Phys. Lett. 110 (2) (2017) 021910.

[57] G. Ackland, R. Thetford, An improved N-body semi-empirical model for body-centred cubic transition metals, Phil. Mag. A 56 (1) (1987) 15–30.

[58] N. Juslin, B.D. Wirth, Interatomic potentials for simulation of He bubble formation in W, J. Nucl. Mater. 432 (1–3) (2013) 61–66.

[59] P. Lejcek, P. Lejček, Grain boundaries: description, structure and thermodynamics, Grain Bound. Segreg. Met. (2010) 5–24.

[60] M. Kotoul, P. Skalka, T. Profant, P. Řehák, P. Šesták, M. Černỳ, J. Pokluda, A novel multiscale approach to brittle fracture of nano/micro-sized components, Fatigue Fract. Eng. Mater. Struct. 43 (8) (2020) 1630–1645.

[61] K. Park, G.H. Paulino, Cohesive zone models: a critical review of traction-separation relationships across fracture surfaces, Appl. Mech. Rev. 64 (6) (2011) 060802.